

Sparsification and Reconstruction from the Perspective of Representation Geometry

Wenjie Sun¹, Bingzhe Wu², Zhile Yang¹, Chengke Wu¹

¹Shenzhen Institute of Advanced Technology, CAS

²Shenzhen University

{wj.sun, zl.yang, ck.wu}@siat.ac.cn, wubingzheagent@gmail.com

Abstract

Sparse Autoencoders (SAEs) have emerged as a predominant tool in mechanistic interpretability, aiming to identify interpretable monosemantic features. However, how does sparse encoding organize the representations of activation vector from language models? What is the relationship between this organizational paradigm and feature disentanglement as well as reconstruction performance? To address these questions, we propose the SAEMA, which validates the stratified structure of the representation by observing the variability of the rank of the symmetric semipositive definite (SSPD) matrix corresponding to the modal tensor unfolded along the latent tensor with the level of noise added to the residual stream. To systematically investigate how sparse encoding alters representational structures, we define local and global representations, demonstrating that they amplify inter-feature distinctions by merging similar semantic features and introducing additional dimensionality. Furthermore, we intervene the global representation from an optimization perspective, proving a significant causal relationship between their separability and the reconstruction performance. This study explains the principles of sparsity from the perspective of representational geometry and demonstrates the impact of changes in representational structure on reconstruction performance. Particularly emphasizes the necessity of understanding representations and incorporating representational constraints, providing empirical references for developing new interpretable tools and improving SAEs. The code is available at <https://github.com/wenjie1835/SAERepGeo>.

1 Introduction

Mechanistic Interpretability (MI) aims to break down neural networks into interpretable components, analyzing their functions and interactions to understand the decision-making mechanisms of the entire network [1–3]. Sparse Autoencoders (SAEs), as a key tool in MI, the initial aim was to address the polysemantic phenomenon caused by feature superposition [4], where neural networks represent more independent features than neurons by assigning each feature a linear combination of neurons [5]. As a neural network implementation of dictionary learning, SAEs decompose input activation vectors into sparse and interpretable features, which often correspond to specific directions in the representation space [5]. To evaluate the effectiveness of this paradigm and provide optimization insights, we must understand how SAEs organize the representation of the activation vector.

A key claim of the linear representation hypothesis is that a model’s state is a sparse linear combination of independent features [4, 6, 7]. Olah et al. [8] suggested that these features may lie on a manifold, where the angles between dictionary vectors of features are small, and adjacent features jointly respond to similar data. This led to the proposal of the feature manifold concept. Engels et al. [9]

further validated this by performing clustering and dimensionality reduction of SAE dictionary elements, discovering circular-shaped, multidimensional features related to months and weekdays.

However, it is unclear whether the representation structure of concepts is formed during the language model’s pre-training process or guided by the encoding mechanism of SAEs. Furthermore, how does the representation structure change during sparse encoding, and what is the relationship between these changes, disentangling polysemantic features, and reconstruction performance? Our work aims to explain the mechanisms of SAEs from the perspective of representation geometry and provide insights for their optimization.

1. Inspired by Shrivastava et al. [10], we represent the latent tensors of SAEs as points on a product manifold of symmetric semipositive definite (SSPD) matrices, where the rank variability of the SSPD matrices reflects the stratification of the manifold. Based on this, we propose the SAEManifoldAnalyzer (SAEMA) to analyze how pre-trained SAEs represent activation vectors corresponding to different concepts in language models. The results demonstrate the prevalence of stratified manifolds, where representations of the same concept are distributed across different manifolds.
2. To understand how sparse encoding alters the representation structure, we define local and global representations, capturing the former by performing dimensionality reduction and clustering separately on the residual streams and the sparsely encoded latent tensors in the representation space. Specifically, sparse encoding reduces feature overlap by merging similar semantic features within local representations and introducing more dimensions into it. This finding reveals how SAEs achieve feature disentanglement to identify monosemantic features.
3. To explore the relationship between the geometric properties of the representation structure and SAEs’ reconstruction performance, we intervene in the geometric relationships among local representations from an optimization perspective. The results show that increased separability between different local representations causally enhances reconstruction performance. This finding underscores the necessity of incorporating geometric constraints into SAE optimization and provides new insights for mitigating the conflict between sparsity and reconstruction fidelity.

2 Representation Geometry Framework

2.1 Sparse Autoencoder

Many recent studies have proposed employing Sparse Autoencoders (SAEs) to extract interpretable features from superposition for model understanding and editing, and the efficiency of this paradigm has been validated [11, 12]. SAEs decompose each activation vector $\mathbf{x} \in \mathbb{R}^n$ into a sparse linear combination of learned feature directions using an overcomplete dictionary ($M \gg n$ basis vectors), transforming the complex activation space into sparse, interpretable representations through an encoder (Equation 1)-decoder (Equation 2) architecture:

$$f(\mathbf{x}) := \sigma(\mathbf{W}_{\text{enc}}\mathbf{x} + \mathbf{b}_{\text{enc}}), \quad (1)$$

$$\hat{\mathbf{x}}(f(\mathbf{x})) := \mathbf{W}_{\text{dec}}f(\mathbf{x}) + \mathbf{b}_{\text{dec}}, \quad (2)$$

where $\mathbf{x} \in \mathbb{R}^n$ denotes the language model’s residual stream activation, $f(\mathbf{x}) \in \mathbb{R}^M$ represents the sparse feature activations, and $\sigma(\cdot)$ is a sparsity-enforcing nonlinearity. The encoder parameters $\mathbf{W}_{\text{enc}} \in \mathbb{R}^{M \times n}$, $\mathbf{b}_{\text{enc}} \in \mathbb{R}^M$ and decoder parameters $\mathbf{W}_{\text{dec}} \in \mathbb{R}^{n \times M}$, $\mathbf{b}_{\text{dec}} \in \mathbb{R}^n$ project between spaces of differing dimensionality. The columns of \mathbf{W}_{dec} (denoted $\{\mathbf{d}_i\}_{i=1}^M$) form a feature dictionary used for reconstruction, with each basis vector \mathbf{d}_i corresponding to a learned interpretable feature.

2.2 SAE Manifold Analyzer (SAEMA)

SAEMA is a manifold learning-based method designed to analyze the manifold structure of concepts encoded by SAEs in language models. Figure 1 illustrates its workflow, which consists of the following three steps: 1) Collecting Residual Streams; 2) Injecting noise and Encoding; 3) Tensor Unfolding and Manifold Analysis.

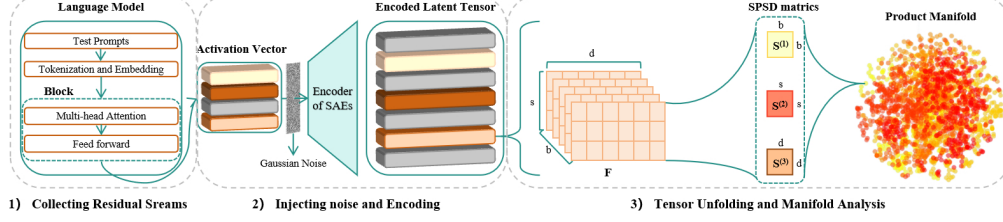


Figure 1: The workflow of SAEManifoldAnalyzer (SAEMA)

Collecting Residual Streams For each model and concept, we extract activation vectors from the specified layer’s residual stream hook (*hook_resid_post*), generating a tensor with shape (*batch_size*, *seq_len*, *d_model*).

Injecting noise and encoding Gaussian white noise is added to the residual stream in a feature-directed manner, with varying intensity levels. High-frequency features (the top 100 based on activation frequency) are perturbed with a noise intensity of $2 \cdot \text{noise_std}$, while the remaining features are subjected to a weaker noise level of $0.2 \cdot \text{noise_std}$. The perturbed residual stream is then processed by a pretrained Sparse Autoencoder (SAE), generating a latent tensor of shape (*batch_size*, *seq_len*, *d_sae*), where d_{sae} denotes the SAE’s feature dimension. To maintain computational efficiency, if d_{sae} exceeds 2048, the tensor is downsampled to 2048 features, selected based on their variance score in Equation 3.

$$\text{score}(j) = \text{Var}(f_j) \cdot \left(\sum_{i \neq j} |\text{Cov}(f_i, f_j)| + \epsilon \right) \quad (3)$$

where $\text{Var}(f_j)$ is the variance of feature j , $\text{Cov}(f_i, f_j)$ is the covariance between features i and j , and ϵ is a small constant to prevent division by zero.

Tensor Unfolding and Manifold Analysis The latent tensor \mathcal{F} is unfolded along three modes (batch, sequence, feature) into matrices $\{F^{(1)}, F^{(2)}, F^{(3)}\}$, and the corresponding SSPD matrices are computed:

$$S^{(i)} = \frac{F^{(i)} F^{(i)T} + (F^{(i)} F^{(i)T})^T}{2} + \epsilon I \quad (4)$$

where $\epsilon = 10^{-5}$ ensures numerical stability. Singular value decomposition is performed on each $S^{(i)}$ to compute its rank:

$$\text{rank}(S^{(i)}) = \sum_{j=1}^n \mathbb{I} \left(\frac{\lambda_j}{\lambda_1} > \tau_i \right) \quad (5)$$

where λ_j are the singular values (in descending order), and τ_i is a dynamic threshold set as the first quartile of effective singular values ($\lambda_j > 10^{-6} \lambda_1$). The rank triplet (r_1, r_2, r_3) characterizes the rank configuration of the latent tensor within the product manifold, reflecting its low-dimensional geometric structure and stability under noise perturbations. The detailed mathematical proof of how the variability of the rank of the SSPD matrix reflects the stratification of the product manifold can be found in the Appendix A.

2.3 Local and Global Representation

A key characteristic of hierarchical manifolds is being locally smooth yet globally non-smooth. To understand how sparse encoding reshapes representational structures comprehensively, we define both local and global representations.

Definition 1(Local Representation). The local representation is a low-dimensional subspace in the SAE latent space, corresponding to a semantically coherent feature cluster \mathcal{C} for a concept, identifiable through clustering, with each cluster described by an SSPD matrix from the feature-mode unfolding. For the latent tensor \mathcal{F} ’s feature-mode $F^{(3)}$, the k -th local representation of concept c is:

$$\mathcal{M}_c^{(k)} = \left\{ \mathbf{z} \in \mathcal{C}_k \mid \text{rank}(S^{(3)}(\mathbf{z})) = r_3^{(k)} \right\}.$$

Definition 2(Global Representation). The global representation is the union of all local representations for a concept, described by a product manifold of SSPD matrices. For concept c , the global representation is:

$$\mathcal{G}_c = \bigcup_{k=1}^K \mathcal{M}_c^{(k)} \subset \prod_{r_3^{(k)}} S_{d_{\text{sae}}}^+(r_3^{(k)}).$$

To quantify the geometric characteristics in local representations, we introduce the average intrinsic dimensionality (Avg. ID) to assess the effective dimensionality occupied by local representations, and Betti 0 to indicate the number of connected components within them. For global representations, we introduce the Minimum Spanning Tree Weight (MSTW), computed as the sum of Euclidean distances between the centers of different local representations, reflecting the overall dispersion of the global representation. Appendix C provides the introduction of these metrics.

3 Experiment Setup

3.1 Model and Dataset

Model We selected the post residual streams from the later layers of three language models for analysis: Layer 11 of GPT2-Small [13], Layer 5 of Pythia-70M [14], and Layer 19 of Gemma2-2B [15], and loaded their corresponding pre-trained SAEs from SAE-Lens [16]. Table 3 and 4 in Appendix B.1 show the detailed configuration of SAEs and language models used in this work.

Dataset We tested six concepts: Months, Weekdays, Chemical Elements, Color, Planets, Number, Alphabet, Phonetic Symbol and constellations. The selection criteria were based on whether their keywords formed clusters in the representation space. For these concepts, we designed diverse and information-dense prompts (Table 5 in Appendix B.1 shows the prompts of Months, Weekdays and Chemical Elements) to capture as complete a representation as possible. The final input to the SAEs was the masked residual stream, filtered of irrelevant tokens (such as prepositions, conjunctions, and <endoftext> et al).

3.2 Experimental Design

In this section, we present three experimental designs to progressively verify our theoretical contributions. Specifically, in Section 3.2.1, we use SAEMA to test the manifold patterns of different concepts across various language models to verify the universality of stratified manifolds. In Section 3.2.2, we perform dimensionality reduction and density-based clustering on both residual stream and latent tensors in the representation space to reveal how sparse encoding modifies the geometric structures of both local and global representations. To investigate the relationship between representation geometry and reconstruction performance, in Section 3.2.3, we perform intervention to the global representations from an optimization perspective, aiming to prove the causal relationship between separability and reconstruction performance.

3.2.1 Case 1: Stratified Manifold

To understand how sparse encoding organizes the representations of activation vectors, we used the SAEMA module to test the representation of all concepts by three SAEs mentioned in Section 3.1 and pre-trained on residual streams of different language models—under varying levels of noise. White Gaussian noise perturbations with nine different standard deviations, ranging from 0.0 to 10.0 (0.0, 0.02, 0.05, 0.1, 0.2, 0.5, 1.0, 2.0, 5.0, 10.0), were added to each of the nine model-concept pairs. To prevent the sparsity constraint of the SAEs from filtering low-frequency activations, we

specifically applied 2x noise to high-frequency activations. By observing the variability of the ranks (r_1, r_2, r_3) of the SSPD matrices corresponding to different modal tensors with respect to noise, to verify whether the latent tensors span manifold layers of different rank configurations.

Evaluation metrics

Rank Variability: The variability of the rank triplet (r_1, r_2, r_3) is examined, with a focus on r_3 (feature mode), to verify if latent representations traverse different manifold strata.

Average Geodesic Distance (AGD): To quantify the continuous geometric differences between SSPD matrices on the manifold and provide supplementary evidence for rank variability, AGD is defined in this paper as the mean geodesic distance of SSPD matrices on the S_n^+ manifold. The specific formula can be found in the Appendix C.

3.2.2 Case 2: Changes in Representation Structure

To investigate the impact of sparse encoding on the structure of representations, we compare representations before (residual stream) and after (SAE latent tensor) sparse encoding. Selecting the same models and three concepts (Months, Weekdays and Chemical Elements) in Case 1. Aiming to reveal the way that sparse encoding organizes representations. The specific experimental steps are as follows:

Dimensionality Reduction: Residual representations $\mathbf{x} \in \mathbb{R}^{batch_size \times seq_len \times d_model}$ and SAE latent tensors $\mathcal{F} \in \mathbb{R}^{batch_size \times seq_len \times d_sae}$ are extracted from the zero-noise cache of Case 1. Representations before and after sparse encoding are first flattened to $\mathbb{R}^{batch_size \times seq_len \times d_sae}$, normalized, and then reduced to 50 dimensions with UMAP, balancing computational efficiency while preserving the structure of the representations as much as possible.

Clustering: HDBSCAN (minimum cluster size = 10) is applied to the dimensionality-reduced representations to identify individual local representations (clusters). We then estimate the intrinsic dimensionality of each local representation and computed its persistent homology to obtain the corresponding Betti 0 (connected components), thereby evaluating the structural changes induced by sparse encoding on local representations. Furthermore, to quantify changes in local representations, we compute the MSTW for both the residual stream and latent tensors, and use Procrustes analysis to compare the geometric rearrangement of the centers of the two sets of local representations before and after sparse encoding. Regarding the formula and definition of Procrustes Disparity can be found in Appendix C.

3.2.3 Case 3: Intervention Representation Structure

To explore the relationship between the geometric structure of latent representations in SAEs and their reconstruction performance, we intervene in the representation structure from an optimization perspective. Inspired by Lee et al. [17] and Nao et al. [18], we employ the Gromov-Wasserstein distance (d_{GW}) to compare the distance metrics of the metric spaces before and after the intervention and incorporate it as an optimization term in the loss function, aim to explore the geometric properties between local representations and reconstruction performance while preserving the representation structure as much as possible. The detailed optimization strategies are as follows:

Procedure: We compute the centers of various local representations of concepts after sparse encoding based on the HDBSCAN cluster labels from Case 2:

$$\mathbf{c}_i = \frac{1}{|\mathcal{C}_i|} \sum_{\mathbf{z} \in \mathcal{C}_i} \mathbf{z}, \quad (6)$$

where \mathcal{C}_i denotes the set of latent representations in cluster i , and $\mathbf{z} \in \mathbb{R}^{d_{sae}}$ is the flattened latent representation with shape $(batch_size \cdot seq_len, d_{sae})$, representing the arithmetic mean of the local semantics of the given concept. The intervention is achieved by translating these centers and their corresponding local representations by different step size α , and the translation direction of was guided by applying stochastic gradients ($grad$) to \mathbf{c}_i to minimize L in Equation.7 during optimization, expressed as $\mathbf{c}'_i \leftarrow \mathbf{c}_i + \alpha \times grad$.

$$L = d_{GW}(D_{original}, D_{intervened}) + \lambda_{MSE} MSE(\mathbf{x}, \hat{\mathbf{x}}) \quad (7)$$

$$d_{\text{GW}}(D_{\text{original}}, D_{\text{intervened}}) = \min_{\pi \in \Pi(\mu, \nu)} \sum_{i,j,i',j'} |D_{\text{original}}(i,j) - D_{\text{intervened}}(i',j')| \pi_{i,i'} \pi_{j,j'} \quad (8)$$

$$D_{\text{original}}(i,j) = \frac{\|\mathbf{z}_i - \mathbf{z}_j\|_2}{\max_{i,j} \|\mathbf{z}_i - \mathbf{z}_j\|_2}, D_{\text{intervened}}(i',j') = \frac{\|\mathbf{z}'_i - \mathbf{z}'_j\|_2}{\max_{i',j'} \|\mathbf{z}'_i - \mathbf{z}'_j\|_2} \quad (9)$$

where d_{GW} in Equation 8 is the GW distance, measuring the structural dissimilarity between the original and intervened latent representations. D_{original} and $D_{\text{intervened}}$ are the normalized Euclidean distance matrices of the original and intervened latent representations, defined in Equation 9. λ_{MSE} is used to control the weight of Mean Squared Error (MSE), set to 1.

Evaluation Metrics: During the optimization process, local representations are translated along with their \mathbf{c}_i , preserving the intra-cluster aggregation degree. To quantify the separability between different local representations, we compute the Average Euclidean Distance between Pairs (AEDP) of cluster centers. The reconstruction performance was quantified by MSE. The detailed introduction about AEDP and MSE can be found in Appendix C.

4 Experimental Results and Analysis

4.1 Case 1

Figure 2 illustrates the variability of r_3 (the rank of SSPD matrix of feature modal) and AGD for three SAEs representing the concepts under different noise levels. Detailed experimental results can be found in Appendix B.2. We observe that the `batch_size` and `seq_len` modal ranks (r_1, r_2) remain constant, which may be attributed to the fact that prompts with high information density and strong semantic consistency stabilize the covariance structure. In contrast, the feature modal rank (r_3) exhibits varying degrees of variability ($SAE_{\text{Pythia-70M Layer 5}}$: 57.37%, $SAE_{\text{GPT2-Small Layer 11}}$: 140.72%, $SAE_{\text{Gemma-2-2B Layer 19}}$: 141.67%), proving that the representational structure of SAEs is stratified.

Additionally, the initial AGD values under zero noise reflect the compactness of the manifolds, showing that larger models tend to have more dispersed representations. The variability of AGD also demonstrates a negative correlation with model scale, the larger the language model, the smaller the AGD variability (Pythia-70M: 145x increase, GPT2-Small: 15.85% increase, Gemma-2-2B: 4.53% increase). This may be attributed to the more dispersed representations mitigating the impact of noise. Regarding the sharp AGD surge in Pythia-70M, may be due to high noise causing geometric collapse in the manifold.

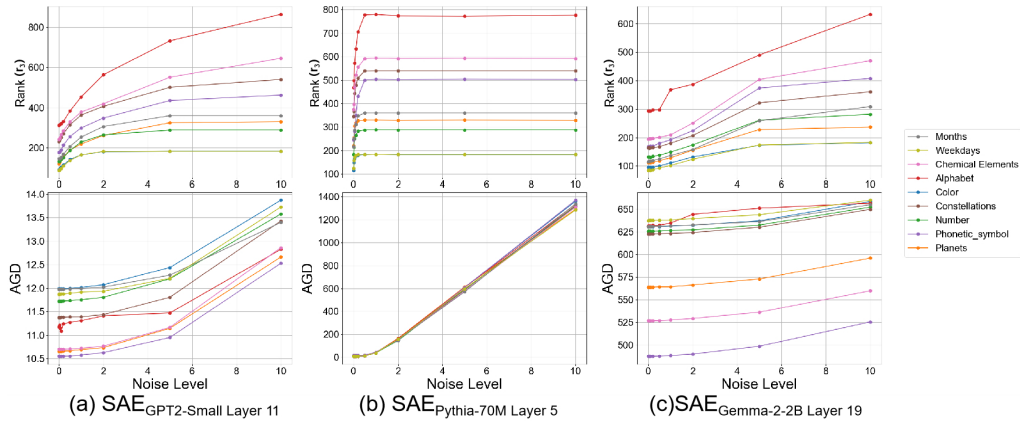


Figure 2: The changes of r_3 and AGD corresponding to different concepts encoded by pre-trained SAEs under different noise levels.

4.2 Case 2

Table 1: Changes in Local and Global Representation Structures Before and After sparse encoding

Model	Concept	Clusters	Local Representation		Global Representation	
			Avg. ID \uparrow	Betti 0 \uparrow	MSTW \downarrow	Procrustes Disparity
GPT2-Small Layer 11	Months	(22, 18)	(3.01, 3.25)	(21.09, 26.11)	(196.57, 101.16)	0.61
	Weekdays	(9, 9)	(3.29, 3.78)	(25.67, 26.00)	(94.57, 73.61)	0.30
	Chemical Elements	(27, 23)	(2.58, 2.86)	(30.74, 36.74)	(119.87, 130.50)	0.63
Pythia-70M Layer 5	Months	(18, 17)	(3.01, 3.15)	(26.67, 28.24)	(165.13, 90.95)	0.52
	Weekdays	(6, 8)	(3.32, 3.81)	(35.83, 27.38)	(59.32, 55.21)	0.15
	Chemical Elements	(22, 26)	(3.19, 2.62)	(34.55, 27.19)	(96.80, 74.80)	0.61
Gemma-2-2B Layer 19	Months	(21, 18)	(2.77, 3.00)	(18.81, 22.00)	(199.27, 113.75)	0.40
	Weekdays	(8, 6)	(3.80, 4.24)	(28.88, 39.67)	(80.46, 67.67)	0.18
	Chemical Elements	(23, 22)	(2.89, 3.13)	(26.45, 27.43)	(172.65, 102.28)	0.53

The cluster counts in Table 1 generally exhibit variability after sparse encoding, with 7 out of 9 model-concept pairs showing a decrease or constant in the number of clusters. Interestingly, the number of clusters also shows a certain positive correlation with the semantic complexity of the concepts (Chemical Elements > Months > Weekdays). For example, concept of chemical element that contains the most keywords corresponds to the largest number of clusters.

Local Representation: Seven out of nine model-concept pairs demonstrate an increase in Avg. ID, indicating that sparse encoding introduces more degrees of freedom into local representations, possibly due to the overcomplete basis vector of SAEs introducing additional feature dimensions. Simultaneously, seven pairs show an increase in Betti 0, i.e., the number of connected components, suggesting that local representations are segmented into more substructures. The increase in Avg. ID and connected components indicates that substructures within the same local representation become more numerous and the differences between substructures become greater, which means the overlap between features is reduced. This phenomenon indirectly explain the mechanism of feature disentanglement. Detailed discussion can be seen in the Appendix B.3.

Global Representation: Since sparse encoding alters the number of local representations, Procrustes analysis was performed considering only the labels of valid clusters. The results demonstrate the universality of topological rearrangement. MSTW serve as a metric to quantify the dispersion of global representations, showed a decreasing trend in 8 out of 9 model-concept pairs, indicating that the global representational structure was compressed during this process. The increase in the Avg. ID of local representations, alongside the compression of global representations, appears contradictory at first glance. However, this suggests that sparse encoding achieves disentanglement solely through effective dimensions, i.e., most dimensions are wasted. It also implies that even with overcomplete basis vector, this approximation method still cannot avoid the representation compression phenomenon of the autoencoder architecture.

4.3 Case 3

Table 2 shows the variations of d_{GW} , MSE, and AEDP for different values of α . All nine model-concept pairs exhibit a trend where AEDP increases and MSE decreases as α increases. This indicates that during the optimization process, the translation directions of each local representation tend to move away from each other, thereby increasing separability. Figure 3 in Appendix B.4.1 shows how AEDP and d_{GW} change as α increases. While increasing α led to an increase in d_{GW} for $SAE_{GPT2-Small\ Layer\ 11}$ and $SAE_{Gemma-2-2B\ Layer\ 19}$, this was not the case for $SAE_{Pythia-70M\ Layer\ 5}$. Interestingly, despite the inconsistent trends of d_{GW} with respect to α across the three models, they consistently show a positive correlation between AEDP and α . This implies that an increase in α does not necessarily lead to an increase in the geometric structure of the representations but directly increases the separability between local representations. Furthermore, Figure 4 in Appendix B.4.1 shows the variations in MSE with respect to AEDP and d_{GW} for different α values. The changes in MSE and d_{GW} do not show a consistent pattern across the three models, but they all consistently exhibit a trend where MSE decreases as AEDP increases. Specifically, the Pearson correlation coefficient between AEDP and MSE is -0.89 for $SAE_{GPT2-Small\ Layer\ 11}$, -0.97 for $SAE_{Pythia-70M\ Layer\ 5}$, and -0.93 for $SAE_{Gemma-2-2B\ Layer\ 19}$, all showing significant negative correlations.

To validate the causal relationship between AEDP and MSE, we modified the loss function in Equation 7 by replacing d_{GW} with $AEDP^{-1}$ while keeping the optimization approach unchanged, as detailed in Appendix B.4.2. The results indicate that the contribution of the $AEDP^{-1}$ term to the total loss is almost negligible. However, MSE and AEDP still exhibit a significant negative correlation. In other words, during optimization, MSE dominates the total loss function to steer local representations away from each other, thereby achieving its own reduction. Based on this, we conclude that the increase in the separability of local representations causally enhances reconstruction performance.

Table 2: Variations of MSE and AEDP corresponding to different translation step sizes (α) during optimization

Conceptual Category	α	SAEGPT2-Small Layer 11				SAEPythia-70M Layer 5				SAEGemma-2-2B Layer 19			
		d_{GW}	MSE↓	Orig. AEDP	AEDP↑	d_{GW}	MSE↓	Orig. AEDP	AEDP↑	d_{GW}	MSE↓	Orig. AEDP	AEDP↑
Months	0.5	0.004	58.09	10.50	11.32	0.071	470.77	7.19	8.21	0.372	44.28	358.97	503.41
	0.8	0.015	55.82	10.50	12.42	0.065	385.93	7.19	9.55	0.401	42.44	358.97	636.98
	1.0	0.027	53.32	10.50	13.33	0.045	329.73	7.19	10.63	0.417	42.20	358.97	731.61
	1.2	0.038	52.61	10.50	14.32	0.031	299.82	7.19	11.79	0.413	40.13	358.97	826.48
	1.5	0.064	48.68	10.50	16.01	0.059	247.75	7.19	13.68	0.420	40.09	358.97	838.85
Weekdays	0.5	0.002	56.04	11.58	12.38	0.073	536.59	7.46	8.48	0.243	41.36	774.53	888.30
	0.8	0.007	54.19	11.58	13.25	0.085	460.20	7.46	9.79	0.258	39.24	774.53	978.66
	1.0	0.014	52.69	11.58	14.29	0.110	440.71	7.46	10.84	0.262	36.56	774.53	1071.95
	1.2	0.030	51.97	11.58	15.29	0.057	386.57	7.46	12.02	0.264	36.09	774.53	1124.52
	1.5	0.052	48.34	11.58	16.91	0.095	331.07	7.46	13.89	0.267	37.96	774.53	1241.20
Chemical Elements	0.5	0.010	51.01	8.49	9.53	0.017	338.21	7.53	8.58	0.310	41.23	318.12	467.12
	0.8	0.027	50.22	8.49	10.81	0.016	309.30	7.53	9.92	0.367	40.57	318.12	604.61
	1.0	0.049	49.23	8.49	11.82	0.011	262.40	7.53	10.99	0.358	40.34	318.12	612.10
	1.2	0.077	48.53	8.49	12.94	0.008	253.90	7.53	12.15	0.370	40.12	318.12	727.67
	1.5	0.109	48.02	8.49	14.78	0.044	244.54	7.53	14.03	0.369	40.23	318.12	699.76

5 Related Work

5.1 Sparse Autoencoder

SAEs, as a critical tool in mechanistic interpretability, aim to address the polysemanticity problem in LLMs caused by feature superposition. However, this paradigm faces several challenges, including shrinkage bias induced by L1 regularization, the trade-off between sparsity and reconstruction fidelity, and the presence of dead features during training. Specifically, shrinkage bias refers to the systematic underestimation of feature activation values by L1 regularization, which degrades reconstruction quality. Rajamanoharan et al. [19] proposed Gated SAE, introducing a gating function and a magnitude estimation function to mitigate this issue. Additionally, the balance between sparsity and reconstruction fidelity limits the scalability of SAEs. To address this, Taggart et al. [20] introduced ProLU SAE, replacing the ReLU activation function with a ProLU activation function that learns dynamic thresholds. Similarly, Rajamanoharan et al. [21] employed the JumpReLU activation function, which sets a fixed activation threshold and uses L0 regularization to control and avoid biases introduced by small activation values. To tackle the inefficiency of dead features and the forced fixed number of activated features for all inputs, Bussmann et al. [22] proposed BatchTopK SAE, which applies TopK selection across the entire batch, allowing different samples to activate varying numbers of features. Ayonrinde et al. [23] ensured feature utilization efficiency by constraining the proportion of samples each feature activates. Significant research has also been devoted to addressing cross-layer challenges in mechanistic interpretability, such as Layer Group SAE [24], which trains shared SAEs by computing activation similarities between layers, and Switch SAE [25], which draws inspiration from the Mixture of Experts framework.

5.2 Representation Geometry

The relationship between representation in latent space and task performance has been well-established in neuroscience[26] and statistical mechanics. Numerous studies have explored language model principles through the lens of representational geometry. For instance, Ethayarajh et al. [27] discovered that contextual representations exhibit anisotropy across all non-input layers and capture semantic information more effectively than static word embeddings. Chang et al. [28] identified stable language-neutral axes in linguistic subspaces across different languages, while Shai et al. [29] demonstrated the linear existence of Belief State Geometry in Transformer residual streams. SAEs trained on language model activation vectors have also revealed intriguing representational structures.

Engles et al. [9], through clustering and dimensionality reduction of dictionary elements, uncovered circular features related to temporal concepts such as days and months. Li et al. [30] identified shared directions for opposing concepts, forming parallelogram structures. Bricken et al. [5] revealed compressed global structures by applying 2D UMAP transformations to SAE encoding directions. However, the geometric transformations during sparse encoding and reconstruction, as well as their relationship to disentanglement, remain insufficiently explored. Given the current substantial research investment in SAEs, we believe it is necessary to provide an optimized reference from the perspective of representation geometry.

5.3 Disentangled Representation Learning

Disentangled representation learning, as a crucial component of unsupervised learning, aims to separate latent factors in data into independent and interpretable representations, thereby enhancing model interpretability [31, 32]. This concept has driven research in natural language processing to disentangle semantic and contextual elements, offering new perspectives on the interpretability and editability of language models. Mairal et al. [33] first introduced the dictionary learning to natural language processing, utilizing overcomplete basis vectors to decompose inputs into sparse linear combinations, generating sparse representations of textual features and laying the foundation for subsequent semantic decomposition.

Regularization serves as a key mechanism for achieving disentanglement [34], prompting researchers to explore additional regularization architectures such as variational autoencoders [35–37] and generative adversarial networks [38–40]. In recent years, SAEs have garnered significant attention due to their sparsity and interpretability in disentangling language model representations. Cunningham et al. [5] pioneered the application of SAEs to LLMs, decomposing activations into sparse, monosemantic features, thereby enhancing interpretability in the era of large language models. With the successful practice of scaling laws, the approximately overcomplete basis vectors in SAEs introduce a conflict between sparsity and reconstruction performance [41]. Moreover, as an unsupervised learning method, the evaluation of feature monosemanticity presents a bottleneck for further replication [42, 43].

6 Conclusion

Our work addresses three key questions sequentially: how sparse coding structures representations, how SAEs achieve feature disentanglement, and the relationship between representational geometry and SAEs reconstruction performance. We observed that SAEs exhibit stratified representations for different concepts within language models, meaning that the representations of the same concept are dispersed across different manifolds. Furthermore, by applying dimensionality reduction and clustering to activation vectors before and after sparse encoding to capture local representations, we find that sparse encoding reduces feature overlap by merging similar semantic features within local representations and introducing more dimensionality, thereby achieving feature disentanglement. Finally, through an optimization-based intervention on the geometric relationships among local representations within the global representation, we significantly improved the reconstruction performance of SAEs without any post-training, demonstrating that increased separability between local representations causally leads to a decrease in reconstruction performance.

In summary, our findings offer guidance for improving SAEs and developing novel tools for decomposing neural networks from the perspective of representation geometry, particularly emphasizing the necessity of understanding and incorporating representation geometry constraints.

References

- [1] L. Sharkey, B. Chughtai, J. Batson, J. Lindsey, J. Wu, L. Bushnaq, N. Goldowsky-Dill, S. Heimersheim, A. Ortega, J. Bloom *et al.*, “Open problems in mechanistic interpretability,” *arXiv preprint arXiv:2501.16496*, 2025.
- [2] L. Bereska and E. Gavves, “Mechanistic interpretability for ai safety—a review,” *arXiv preprint arXiv:2404.14082*, 2024.
- [3] A. Conmy, A. Mavor-Parker, A. Lynch, S. Heimersheim, and A. Garriga-Alonso, “Towards automated circuit discovery for mechanistic interpretability,” *Advances in Neural Information Processing Systems*, vol. 36, pp. 16 318–16 352, 2023.
- [4] N. Elhage, T. Hume, C. Olsson, N. Schiefer, T. Henighan, S. Kravec, Z. Hatfield-Dodds, R. Lasenby, D. Drain, C. Chen *et al.*, “Toy models of superposition,” *arXiv preprint arXiv:2209.10652*, 2022.
- [5] T. Bricken, A. Templeton, J. Batson, B. Chen, A. Jermyn, T. Conerly, N. Turner, C. Anil, C. Denison, A. Askell *et al.*, “Towards monosemanticity: Decomposing language models with dictionary learning,” *Transformer Circuits Thread*, vol. 2, 2023.
- [6] K. Park, Y. J. Choe, and V. Veitch, “The linear representation hypothesis and the geometry of large language models,” *arXiv preprint arXiv:2311.03658*, 2023.
- [7] Y. Jiang, G. Rajendran, P. Ravikumar, B. Aragam, and V. Veitch, “On the origins of linear representations in large language models,” *arXiv preprint arXiv:2403.03867*, 2024.
- [8] O. Chris and J. Batson, “Feature manifold toy model,” 2023. [Online]. Available: <https://transformer-circuits.pub/2023/may-update/index.html#feature-manifolds>
- [9] J. Engels, E. J. Michaud, I. Liao, W. Gurnee, and M. Tegmark, “Not all language model features are one-dimensionally linear,” 2025. [Online]. Available: <https://arxiv.org/abs/2405.14860>
- [10] A. Shrivastava, R. Rameshan, and S. Agnihotri, “Latent space characterization of autoencoder variants,” *arXiv preprint arXiv:2412.04755*, 2024.
- [11] Y. Zhao, A. Devoto, G. Hong, X. Du, A. P. Gema, H. Wang, X. He, K.-F. Wong, and P. Minervini, “Steering knowledge selection behaviours in llms via sae-based representation engineering,” *arXiv preprint arXiv:2410.15999*, 2024.
- [12] C. Kissane, R. Krzyzanowski, J. I. Bloom, A. Conmy, and N. Nanda, “Interpreting attention layer outputs with sparse autoencoders,” *arXiv preprint arXiv:2406.17759*, 2024.
- [13] A. Radford, J. Wu, R. Child, D. Luan, D. Amodei, I. Sutskever *et al.*, “Language models are unsupervised multitask learners,” *OpenAI blog*, vol. 1, no. 8, p. 9, 2019.
- [14] S. Biderman, H. Schoelkopf, Q. G. Anthony, H. Bradley, K. O’Brien, E. Hallahan, M. A. Khan, S. Purohit, U. S. Prashanth, E. Raff *et al.*, “Pythia: A suite for analyzing large language models across training and scaling,” in *International Conference on Machine Learning*. PMLR, 2023, pp. 2397–2430.
- [15] G. Team, M. Riviere, S. Pathak, P. G. Sessa, C. Hardin, S. Bhupatiraju, L. Hussenot, T. Mesnard, B. Shahriari, A. Ramé *et al.*, “Gemma 2: Improving open language models at a practical size,” *arXiv preprint arXiv:2408.00118*, 2024.
- [16] C. T. Joseph Bloom and D. Chanin, “Saelens,” <https://github.com/jbloomAus/SAELens>, 2024.
- [17] W. Lee, R. C. O’Neill, D. Zou, J. Calder, and G. Lerman, “Geometry-preserving encoder/decoder in latent generative models,” *arXiv preprint arXiv:2501.09876*, 2025.
- [18] N. Nakagawa, R. Togo, T. Ogawa, and M. Haseyama, “Gromov-Wasserstein autoencoders,” in *Proceedings of International Conference on Learning Representations (ICLR)*, 2023. [Online]. Available: <https://openreview.net/forum?id=sbS10BCtc7>
- [19] S. Rajamanoharan, A. Conmy, L. Smith, T. Lieberum, V. Varma, J. Kramár, R. Shah, and N. Nanda, “Improving dictionary learning with gated sparse autoencoders,” *arXiv preprint arXiv:2404.16014*, 2024.
- [20] G. M. Taggart, “Prolu: A nonlinearity for sparse autoencoders,” <https://www.alignmentforum.org/posts/HEpufTdakGTTKgoYF/prolu-a-nonlinearity-for-sparse-autoencoders>, 2024.
- [21] N. B. Erichson, Z. Yao, and M. W. Mahoney, “Jumprelu: A retrofit defense strategy for adversarial attacks,” *arXiv preprint arXiv:1904.03750*, 2019.

- [22] B. Bussmann, P. Leask, and N. Nanda, “Batchtopk sparse autoencoders,” *arXiv preprint arXiv:2412.06410*, 2024.
- [23] K. Ayonrinde, “Adaptive sparse allocation with mutual choice & feature choice sparse autoencoders,” *arXiv preprint arXiv:2411.02124*, 2024.
- [24] D. Ghilardi, F. Belotti, and M. Molinari, “Efficient training of sparse autoencoders for large language models via layer groups,” *arXiv preprint arXiv:2410.21508*, 2024.
- [25] A. Mudide, J. Engels, E. J. Michaud, M. Tegmark, and C. S. de Witt, “Efficient dictionary learning with switch sparse autoencoders,” *arXiv preprint arXiv:2410.08201*, 2024.
- [26] R. Srinath, A. M. Ni, C. Marucci, M. R. Cohen, and D. H. Brainard, “Orthogonal neural representations support perceptual judgments of natural stimuli,” *Scientific Reports*, vol. 15, no. 1, p. 5316, 2025.
- [27] K. Ethayarajh, “How contextual are contextualized word representations? comparing the geometry of bert, elmo, and gpt-2 embeddings,” *arXiv preprint arXiv:1909.00512*, 2019.
- [28] T. A. Chang, Z. Tu, and B. K. Bergen, “The geometry of multilingual language model representations,” *ArXiv*, vol. abs/2205.10964, 2022. [Online]. Available: <https://api.semanticscholar.org/CorpusID:248987203>
- [29] A. Shai, L. Teixeira, A. Oldenziel, S. Marzen, and P. Riechers, “Transformers represent belief state geometry in their residual stream,” *Advances in Neural Information Processing Systems*, vol. 37, pp. 75 012–75 034, 2024.
- [30] Y. Li, E. J. Michaud, D. D. Baek, J. Engels, X. Sun, and M. Tegmark, “The geometry of concepts: Sparse autoencoder feature structure,” *arXiv preprint arXiv:2410.19750*, 2024.
- [31] Y. Bengio, A. Courville, and P. Vincent, “Representation learning: A review and new perspectives,” *IEEE transactions on pattern analysis and machine intelligence*, vol. 35, no. 8, pp. 1798–1828, 2013.
- [32] I. Higgins, L. Matthey, A. Pal, C. Burgess, X. Glorot, M. Botvinick, S. Mohamed, and A. Lerchner, “beta-vae: Learning basic visual concepts with a constrained variational framework,” in *International conference on learning representations*, 2017.
- [33] J. Mairal, F. Bach, J. Ponce, and G. Sapiro, “Online dictionary learning for sparse coding,” in *Proceedings of the 26th annual international conference on machine learning*, 2009, pp. 689–696.
- [34] X. Wang, H. Chen, Z. Wu, W. Zhu *et al.*, “Disentangled representation learning,” *IEEE Transactions on Pattern Analysis and Machine Intelligence*, 2024.
- [35] J. Xu, Y. Ren, H. Tang, X. Pu, X. Zhu, M. Zeng, and L. He, “Multi-vae: Learning disentangled view-common and view-peculiar visual representations for multi-view clustering,” in *Proceedings of the IEEE/CVF international conference on computer vision*, 2021, pp. 9234–9243.
- [36] E. Mathieu, T. Rainforth, N. Siddharth, and Y. W. Teh, “Disentangling disentanglement in variational autoencoders,” in *International conference on machine learning*. PMLR, 2019, pp. 4402–4412.
- [37] Z. Ding, Y. Xu, W. Xu, G. Parmar, Y. Yang, M. Welling, and Z. Tu, “Guided variational autoencoder for disentanglement learning,” in *Proceedings of the IEEE/CVF conference on computer vision and pattern recognition*, 2020, pp. 7920–7929.
- [38] B. Liu, Y. Zhu, Z. Fu, G. De Melo, and A. Elgammal, “Oogan: Disentangling gan with one-hot sampling and orthogonal regularization,” in *Proceedings of the AAAI Conference on Artificial Intelligence*, vol. 34, no. 04, 2020, pp. 4836–4843.
- [39] M. Baas and H. Kamper, “Disentanglement in a gan for unconditional speech synthesis,” *IEEE/ACM Transactions on Audio, Speech, and Language Processing*, vol. 32, pp. 1324–1335, 2024.
- [40] G. Kwon and J. C. Ye, “Diagonal attention and style-based gan for content-style disentanglement in image generation and translation,” in *Proceedings of the IEEE/CVF International Conference on Computer Vision*, 2021, pp. 13 980–13 989.
- [41] A. Mudide, J. Engels, E. J. Michaud, M. Tegmark, and C. S. de Witt, “Efficient dictionary learning with switch sparse autoencoders,” *arXiv preprint arXiv:2410.08201*, 2024.
- [42] M. Bhan, Y. Choho, P. Moreau, J.-N. Vittaut, N. Chesneau, and M.-J. Lesot, “Towards achieving concept completeness for unsupervised textual concept bottleneck models,” *arXiv preprint arXiv:2502.11100*, 2025.

- [43] A. Karvonen, B. Wright, C. Rager, R. Angell, J. Brinkmann, L. Smith, C. Mayrink Verdun, D. Bau, and S. Marks, “Measuring progress in dictionary learning for language model interpretability with board game models,” *Advances in Neural Information Processing Systems*, vol. 37, pp. 83 091–83 118, 2024.
- [44] Z. Liu, J. Gore *et al.*, “Superposition yields robust neural scaling,” *arXiv preprint arXiv:2505.10465*, 2025.
- [45] L. Amsaleg, O. Chelly, T. Furon, S. Girard, M. E. Houle, K.-i. Kawarabayashi, and M. Nett, “Estimating local intrinsic dimensionality,” in *Proceedings of the 21th ACM SIGKDD International Conference on Knowledge Discovery and Data Mining*, 2015, pp. 29–38.
- [46] J. Ma and F. Zheng, “Geometrically bounding 3-manifolds, volume and betti numbers,” *Algebraic & Geometric Topology*, vol. 23, no. 3, pp. 1055–1096, 2023.
- [47] Y. Wang, S. Yu, Y. Gu, and J. Shun, “Fast parallel algorithms for euclidean minimum spanning tree and hierarchical spatial clustering,” in *Proceedings of the 2021 international conference on management of data*, 2021, pp. 1982–1995.
- [48] X. Zeng, “Applications of average geodesic distance in manifold learning,” in *International Conference on Rough Sets and Knowledge Technology*. Springer, 2008, pp. 540–547.
- [49] D. Shu, X. Wu, H. Zhao, D. Rai, Z. Yao, N. Liu, and M. Du, “A survey on sparse autoencoders: Interpreting the internal mechanisms of large language models,” *arXiv preprint arXiv:2503.05613*, 2025.

Appendix

Appendix Contents

A Proof: The variability of $\text{Rank}(S^{(i)})$ reflects product manifold stratification	13
B Experimental Details and Results	14
B.1 Datasets and Configurations	14
B.2 Experiment Results of Case 1	14
B.3 Discussion of the results of the experiment in Case 2	18
B.4 Experiment Results of Case 3	18
C Evaluation Metrics	20
D Limitations	21
E Impact Statement	21
F Reproducibility	21

A Proof: The variability of $\text{Rank}(S^{(i)})$ reflects product manifold stratification

For latent tensor $\mathcal{F} \in \mathbb{R}^{I_1 \times I_2 \times I_3}$, where $I_1 = \text{batch_size}$, $I_2 = \text{seq_len}$, and $I_3 = d_{\text{sae}}$. The mode- i unfolding $F^{(i)}$ is a matrix obtained by arranging the fibers of \mathcal{F} along mode i . For example, $F^{(3)} \in \mathbb{R}^{I_3 \times (I_1 I_2)}$ stacks all feature vectors across batch and sequence dimensions.

The SSPD matrix is defined as:

$$S^{(i)} = \frac{F^{(i)} F^{(i)T} + (F^{(i)} F^{(i)T})^T}{2} + \epsilon I = F^{(i)} F^{(i)T} + \epsilon I,$$

where $\epsilon = 10^{-5}$ ensures numerical stability, and the symmetry follows since $(F^{(i)} F^{(i)T})^T = F^{(i)} F^{(i)T}$.

Since ϵI is a small perturbation, the rank of $S^{(i)}$ approximates the rank of $F^{(i)} F^{(i)T}$. By properties of matrix products, $\text{rank}(F^{(i)} F^{(i)T}) = \text{rank}(F^{(i)})$, because $F^{(i)T}$ maps the row space of $F^{(i)}$ to itself. Thus:

$$r_i = \text{rank}(S^{(i)}) \approx \text{rank}(F^{(i)}).$$

The $\text{rank}(F^{(i)})$ is the dimension of the column space of $F^{(i)}$, which represents the subspace spanned by the mode- i fibers of \mathcal{F} . For mode 3 (features), $F^{(3)}$ contains feature vectors across all tokens, and $\text{rank}(F^{(3)})$ is the number of linearly independent feature directions, reflecting the effective dimensionality of the latent feature space. Thus, r_i characterizes the effective dimension of the mode- i subspace of \mathcal{F} , and the triplet (r_1, r_2, r_3) defines the geometric structure of \mathcal{F} on the product manifold $S_{I_1}(r_1) \times S_{I_2}(r_2) \times S_{I_3}(r_3)$.

For the latent tensor $\mathcal{F} \in \mathbb{R}^{I_1 \times I_2 \times I_3}$, with mode- i unfolding $F^{(i)}$, and SSPD matrix $S^{(i)} = F^{(i)} F^{(i)T} + \epsilon I$. The rank $r_i = \text{rank}(S^{(i)}) \approx \text{rank}(F^{(i)})$ is the dimension of the mode- i subspace. The product manifold is:

$$\mathcal{M} = S_{I_1}(r_1) \times S_{I_2}(r_2) \times S_{I_3}(r_3),$$

where $S_{I_i}(r_i)$ is the manifold of $I_i \times I_i$ SSPD matrices of rank r_i .

A stratified manifold is a union of smooth submanifolds (strata) of different dimensions, i.e., $\mathcal{M} = \bigcup_{r_1, r_2, r_3} S_{I_1}(r_1) \times S_{I_2}(r_2) \times S_{I_3}(r_3)$, where each stratum corresponds to a unique rank triplet (r_1, r_2, r_3) . If \mathcal{F} lies on a single smooth manifold, the rank triplet remains constant under perturbations. If the ranks vary, \mathcal{F} traverses different strata, indicating stratification.

We perturb the residual stream $\mathbf{x} \in \mathbb{R}^{I_1 \times I_2 \times d_{\text{model}}}$ with Gaussian noise $\mathcal{N}(0, \sigma^2)$, producing $\mathbf{x}' = \mathbf{x} + \eta$, where $\eta \sim \mathcal{N}(0, \sigma^2)$ and $\sigma \in \{0, 0.02, \dots, 10\}$. The SAE encodes \mathbf{x}' into \mathcal{F}' , with unfolding $F'^{(i)}$. The SSPD matrix becomes:

$$S'^{(i)} = F'^{(i)} F'^{(i)T} + \epsilon I.$$

Assume $F^{(i)}$ has rank r_i . Noise η perturbs the column space of $F^{(i)}$, potentially increasing $\text{rank}(F'^{(i)})$ by activating additional linearly independent directions. For the feature mode ($i = 3$), $F^{(3)} \in \mathbb{R}^{I_3 \times (I_1 I_2)}$ represents feature vectors. Noise may activate sparse features in the SAE, increasing the number of active directions, thus:

$$r'_3 = \text{rank}(F'^{(3)}) \geq r_3.$$

In other word, the variability of r_3 under noise reflects transitions across submanifolds $S_{I_3}(r_3)$, confirming that the latent space is a stratified manifold.

B Experimental Details and Results

B.1 Datasets and Configuration

To verify the stratification of the manifolds representing concepts in the latent space of SAEs, we tested the SAEMA on SAEs pre-trained on the residual streams of three different language models. The concepts tested were "Months", "Weekdays", "Chemical Elements", "Alphabet", "Color", "Constellations", "Number", "Phonetic Symbol", and "Planets", and the noise levels ranging from 0.0, 0.02, 0.05, 0.1, 0.2, 0.5, 1.0, 2.0, 5.0, to 10.0. To mitigate dead activations and ensure as many features as possible responded, we designed diverse prompts for each concept, Table 5 shows the prompts of "Months", "Weekdays", "Chemical Elements", Table 4 shows the basic configurations of the language models and Table 3 shows the corresponding configurations of the pretrained SAEs that loaded from SAE-Lens.

Table 3: Configuration of the Pretrained SAEs

Property	GPT2-Small Layer 11	Pythia-70M Layer 5	Gemma-2-2B Layer 19
Model Name	gpt2-small	EleutherAI/pythia-70m-deduped	gemma-2-2b
Release	gpt2-small-resid-post-v5-32k	pythia-70m-deduped-res-sm	sae_bench_gemma-2-2b_topk_width-2pow16_date-1109
SAE ID	blocks.11.hook_resid_post	blocks.5.hook_resid_post	blocks.19.hook_resid_post_trainer_0
Hook Point	blocks.11.hook_resid_post	blocks.5.hook_resid_post	blocks.19.hook_resid_post
Context Size	128	128	128
d_{sae}	32,768	32,768	65,536
$d_{\text{sae}}/d_{\text{model}}$	42.7	64.0	28.4
Batch Size	4096	4096	4096

Table 4: Configuration of the language models corresponding to the SAEs

Property	GPT2-Small Layer 11	Pythia-70M Layer 5	Gemma-2-2B Layer 19
Parameter Count	124M	70M	2.2B
Number of Layers	12	6	26
Hidden Dimension (d_{model})	768	512	2304
Number of Attention Heads	12	8	16
Maximum Sequence Length	1024	2048	8192
Vocabulary Size	50257	50304	256000
Position Embedding Type	Learned	Rotary	Rotary
Pretraining Framework	Transformers (Hugging Face)	GPT-NeoX (EleutherAI)	Transformers (Hugging Face)

B.2 Experiment Results of Case 1

The variation of the rank of the SSPD matrices and Average Geodesic Distance (AGD) corresponding to the modal matrices unfolded along the three dimensions with different noise levels is shown in Table 6 and 7.

Table 5: Prompts of Months, Weekdays and Chemical Elements

Concept	Prompt
Months	"January", "February", "March", "April", "May", "June", "July", "August", "September", "October", "November", "December", "January starts the year.", "February follows January.", "March comes after February.", "April is the fourth month.", "May succeeds April.", "June marks midyear.", "July is the seventh month.", "August follows July.", "September begins the fall.", "October is the tenth month.", "November nears year-end.", "December ends the year.", "January in winter.", "February in winter.", "March in spring.", "April in spring.", "May in spring.", "June in summer.", "July in summer.", "August in summer.", "September in fall.", "October in fall.", "November in fall.", "December in winter.", "Month one is January.", "Month two is February.", "Month three is March.", "Month four is April.", "Month five is May.", "Month six is June.", "Month seven is July.", "Month eight is August.", "Month nine is September.", "Month ten is October.", "Month eleven is November.", "Month twelve is December.", "The month of January.", "The month of February.", "The month of March.", "The month of April.", "The month of May.", "The month of June.", "The month of July.", "The month of August.", "The month of September.", "The month of October.", "The month of November.", "The month of December."
Weekdays	"Monday", "Tuesday", "Wednesday", "Thursday", "Friday", "Saturday", "Sunday", "Monday starts the week.", "Tuesday follows Monday.", "Wednesday comes after Tuesday.", "Thursday is the fourth day.", "Friday succeeds Thursday.", "Saturday marks the weekend.", "Sunday ends the week.", "Monday in workweek.", "Tuesday in workweek.", "Wednesday in workweek.", "Thursday in workweek.", "Friday in workweek.", "Saturday in weekend.", "Sunday in weekend.", "Day one is Monday.", "Day two is Tuesday.", "Day three is Wednesday.", "Day four is Thursday.", "Day five is Friday.", "Day six is Saturday.", "Day seven is Sunday.", "The day of Monday.", "The day of Tuesday.", "The day of Wednesday.", "The day of Thursday.", "The day of Friday.", "The day of Saturday.", "The day of Sunday."
Chemical Elements	"Hydrogen", "Helium", "Lithium", "Beryllium", "Boron", "Carbon", "Nitrogen", "Oxygen", "Fluorine", "Neon", "Sodium", "Magnesium", "Hydrogen starts the periodic table.", "Helium follows Hydrogen.", "Lithium comes after Helium.", "Beryllium is the fourth element.", "Boron succeeds Beryllium.", "Carbon follows Boron.", "Nitrogen comes after Carbon.", "Oxygen succeeds Nitrogen.", "Fluorine follows Oxygen.", "Neon comes after Fluorine.", "Sodium starts the third period.", "Magnesium follows Sodium.", "Hydrogen is a non-metal.", "Helium is a noble gas.", "Lithium is an alkali metal.", "Beryllium is an alkaline earth metal.", "Boron is a metalloid.", "Carbon forms life.", "Nitrogen is in air.", "Oxygen supports life.", "Fluorine is highly reactive.", "Neon glows in signs.", "Sodium is in salt.", "Magnesium burns brightly.", "Hydrogen in period one.", "Helium in period one.", "Lithium in period two.", "Beryllium in period two.", "Boron in period two.", "Carbon in period two.", "Nitrogen in period two.", "Oxygen in period two.", "Fluorine in period two.", "Neon in period two.", "Sodium in period three.", "Magnesium in period three.", "Element one is Hydrogen.", "Element two is Helium.", "Element three is Lithium.", "Element four is Beryllium.", "Element five is Boron.", "Element six is Carbon.", "Element seven is Nitrogen.", "Element eight is Oxygen.", "Element nine is Fluorine.", "Element ten is Neon.", "Element eleven is Sodium.", "Element twelve is Magnesium.", "The element of Hydrogen.", "The element of Helium.", "The element of Lithium.", "The element of Beryllium.", "The element of Boron.", "The element of Carbon.", "The element of Nitrogen.", "The element of Oxygen.", "The element of Fluorine.", "The element of Neon.", "The element of Sodium.", "The element of Magnesium."

Table 6: Ranks of the SSPD matrix (r_1, r_2, r_3) and AGD values for pre-trained SAEs across three concepts (**Months**, **Weekdays**, **Chemical Elements**) under varying noise levels.

Concept	Noise Level	<i>SAE_{GPT2-Small}</i> Layer 11				<i>SAE_{Pythia-70M}</i> Layer 5				<i>SAE_{Gemma-2-2B}</i> Layer 19			
		r_1	r_2	r_3	AGD	r_1	r_2	r_3	AGD	r_1	r_2	r_3	AGD
Months	0.00	45	6	146	11.97	45	6	216	8.33	45	5	118	1319.10
	0.02	45	6	147	11.97	45	6	251	8.34	45	5	119	1319.24
	0.05	45	6	149	11.97	45	6	290	8.38	45	5	120	1319.53
	0.10	45	6	155	11.98	45	6	309	8.46	45	5	125	1319.79
	0.20	45	6	165	11.98	45	6	346	8.69	45	5	129	1320.09
	0.50	45	6	207	11.98	45	6	360	12.08	45	5	144	1320.87
	1.00	45	6	251	12.00	45	6	360	36.58	45	5	162	1321.62
	2.00	45	6	305	12.02	45	6	359	157.30	45	5	174	1322.93
	5.00	45	6	360	12.21	45	6	360	572.87	45	5	196	1327.87
	10.00	45	6	360	13.46	45	6	360	1262.54	45	5	237	1355.26
Weekdays	0.00	26	5	88	11.87	26	5	124	9.41	26	5	82	1304.22
	0.02	26	5	89	11.87	26	5	159	9.43	26	5	82	1304.28
	0.05	26	5	93	11.88	26	5	171	9.43	26	5	85	1304.61
	0.10	26	5	100	11.88	26	5	181	9.55	26	5	89	1304.88
	0.20	26	5	108	11.88	26	5	183	9.77	26	5	95	1305.37
	0.50	26	5	141	11.89	26	5	183	12.95	26	5	107	1305.97
	1.00	26	5	163	11.89	26	5	183	42.71	26	5	114	1306.61
	2.00	26	5	182	11.95	26	5	183	149.61	26	5	120	1307.61
	5.00	26	5	183	12.32	26	5	183	570.94	26	5	138	1317.50
	10.00	26	5	183	13.56	26	5	183	1348.77	26	5	165	1338.49
Chemical Elements	0.00	54	9	241	10.70	54	8	375	9.46	54	6	179	1171.65
	0.02	54	9	245	10.70	54	8	397	9.47	54	6	180	1171.74
	0.05	54	9	250	10.70	54	8	469	9.49	54	6	180	1171.90
	0.10	54	9	266	10.70	54	8	521	9.54	54	6	185	1172.07
	0.20	54	9	285	10.70	54	8	555	9.81	54	6	189	1172.29
	0.50	54	9	330	10.70	54	8	591	13.44	54	6	201	1172.82
	1.00	54	9	378	10.72	54	8	594	40.58	54	6	222	1173.63
	2.00	54	9	419	10.77	54	8	592	153.71	54	6	240	1174.72
	5.00	54	9	551	11.17	54	8	593	578.41	54	6	261	1183.68
	10.00	54	9	645	12.86	54	8	592	1309.70	54	6	320	1203.08

Table 7: Ranks of the SSPD matrix (r_1 , r_2 , r_3) and AGD values for pre-trained SAEs across six concepts (**Alphabet**, **Color**, **Constellations**, **Number**, **Phonetic Symbol**, **Planets**) under varying noise levels.

Concept	Noise Level	<i>SAE_{GPT2-Small}</i> Layer 11				<i>SAE_{Pythia-70M}</i> Layer 5				<i>SAE_{Gemma-2-2B}</i> Layer 19			
		r_1	r_2	r_3	AGD	r_1	r_2	r_3	AGD	r_1	r_2	r_3	AGD
Alphabet	0.00	97	6	312	11.17	97	6	468	8.63	97	6	294	631.31
	0.02	97	6	314	11.21	97	6	498	8.67	97	6	294	631.31
	0.05	97	6	316	11.15	97	6	572	8.66	97	6	294	631.32
	0.10	97	6	321	11.09	97	6	633	8.69	97	6	294	631.32
	0.20	97	6	331	11.24	97	6	705	9.01	97	6	297	632.21
	0.50	97	6	383	11.28	97	6	778	12.45	97	6	298	632.21
	1.00	97	6	453	11.31	97	6	780	38.04	97	6	368	634.57
	2.00	97	6	563	11.41	97	6	773	163.13	97	6	387	644.17
	5.00	97	6	732	11.47	97	6	772	608.19	97	6	490	650.92
	10.00	97	6	864	12.82	97	6	776	1334.49	97	6	633	656.45
Color	0.00	26	5	91	11.99	26	5	116	9.05	26	5	96	630.61
	0.02	26	5	93	11.99	26	5	149	9.06	26	5	95	630.61
	0.05	26	5	97	11.99	26	5	168	9.07	26	5	95	630.62
	0.10	26	5	105	11.99	26	5	177	9.11	26	5	96	630.61
	0.20	26	5	115	11.99	26	5	181	9.45	26	5	96	630.68
	0.50	26	5	142	12.00	26	5	183	12.76	26	5	101	630.81
	1.00	26	5	165	12.01	26	5	184	39.83	26	5	111	631.33
	2.00	26	5	181	12.07	26	5	183	149.47	26	5	132	632.19
	5.00	26	5	183	12.44	26	5	183	609.77	26	5	173	637.02
	10.00	26	5	183	13.87	26	5	183	1360.58	26	5	182	658.20
Constellations	0.00	54	7	231	11.38	54	7	345	9.32	54	5	164	622.75
	0.02	54	7	237	11.38	54	7	368	9.32	54	5	165	622.77
	0.05	54	7	244	11.38	54	7	443	9.34	54	5	163	622.78
	0.10	54	7	252	11.38	54	7	478	9.41	54	5	164	622.78
	0.20	54	7	269	11.38	54	7	509	9.69	54	5	165	622.77
	0.50	54	7	315	11.39	54	7	539	12.92	54	5	168	622.85
	1.00	54	7	363	11.39	54	7	540	39.70	54	5	180	623.08
	2.00	54	7	406	11.44	54	7	540	154.04	54	5	207	624.13
	5.00	54	7	501	11.81	54	7	539	617.11	54	5	322	629.99
	10.00	54	7	540	13.43	54	7	540	1322.80	54	5	361	649.63
Number	0.00	41	5	132	11.72	41	5	184	8.87	41	5	132	625.66
	0.02	41	5	132	11.72	41	5	215	8.88	41	5	132	625.67
	0.05	41	5	135	11.72	41	5	251	8.91	41	5	132	625.66
	0.10	41	5	144	11.72	41	5	265	8.96	41	5	131	625.70
	0.20	41	5	152	11.73	41	5	283	9.22	41	5	135	625.71
	0.50	41	5	187	11.74	41	5	288	12.39	41	5	138	625.85
	1.00	41	5	229	11.75	41	5	289	37.19	41	5	149	626.41
	2.00	41	5	264	11.81	41	5	288	145.61	41	5	174	627.09
	5.00	41	5	288	12.20	41	5	288	588.49	41	5	261	632.37
	10.00	41	5	288	13.58	41	5	288	1317.34	41	5	282	652.09
Phonetic Symbol	0.00	42	8	177	10.55	42	9	246	14.56	42	7	168	487.41
	0.02	42	8	179	10.55	42	9	250	14.57	42	7	169	487.42
	0.05	42	8	180	10.55	42	9	281	14.58	42	7	169	487.43
	0.10	42	8	190	10.55	42	9	349	14.65	42	7	170	487.45
	0.20	42	8	213	10.56	42	9	431	14.93	42	7	170	487.46
	0.50	42	8	256	10.56	42	9	500	18.19	42	7	180	487.68
	1.00	42	8	299	10.58	42	9	504	44.25	42	7	192	488.24
	2.00	42	8	348	10.63	42	9	502	149.26	42	7	224	489.80
	5.00	42	8	435	10.95	42	9	504	608.31	42	7	374	498.49
	10.00	42	8	462	12.53	42	9	503	1369.46	42	7	408	525.42
Planets	0.00	30	8	121	10.66	30	8	220	8.59	30	6	113	563.82
	0.02	30	8	128	10.66	30	8	255	8.59	30	6	113	563.83
	0.05	30	8	132	10.66	30	8	305	8.62	30	6	114	563.82
	0.10	30	8	145	10.66	30	8	319	8.69	30	6	113	563.81
	0.20	30	8	154	10.66	30	8	327	9.03	30	6	114	563.84
	0.50	30	8	189	10.67	30	8	330	12.95	30	6	119	564.08
	1.00	30	8	219	10.69	30	8	330	39.84	30	6	129	564.13
	2.00	30	8	261	10.73	30	8	329	164.59	30	6	156	566.21
	5.00	30	8	325	11.15	30	8	330	613.29	30	6	228	572.72
	10.00	30	8	330	12.66	30	8	329	1290.54	30	6	237	595.88

B.3 Discussion of the results of the experiment in Case 2

Liu et al. [44] pointed out that the superposition phenomenon is a key mechanism behind scaling laws—that is, the larger the model scale, the more pronounced the superposition phenomenon. As the smallest of the three language models, Pythia 70M exhibits the weakest superposition, indicating that the overlap in local features is not severe. Moreover, as shown in Table 3, the expansion factor of *SAE Pythia 70M Layer 5* is 64.0, indicating the highest level of sparsity. Therefore, among the three concepts represented by *SAE Pythia 70M Layer 5*, the number of connected components decreases for two of them, which may be due to the weaker feature overlap within its local representations, resulting in a separation trend that is less dominant than the merging of similar semantics.

If the degree of feature overlap in local representations is taken as an indirect indicator of decoupling, then both the increase in *Avg. ID* accompanied by an increase in *Betti 0* in large-scale models and the increase in *Avg. ID* accompanied by a decrease in *Betti 0* in small-scale models could indirectly suggest a reduction in feature overlap—that is, the successful separation of monosemantic features.

B.4 Experiment Results of Case 3

B.4.1 Visualization Results of the Optimization Process based on Equation 7

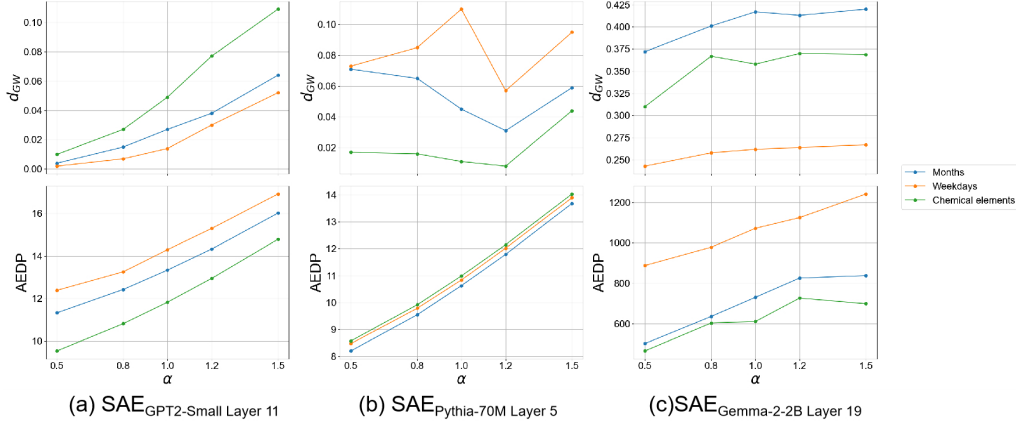


Figure 3: Variability of d_{GW} and AEDP with increasing α during the optimization of Equation 7.

B.4.2 Experiment Details and Results of the Optimization Process based on Equation 10

To validate the causal relationship between the separability of the proposed local representations and the reconstruction performance of SAE, we modified the loss function in Equation 7 by replacing d_{GW} with $AEDP^{-1}$, as shown in Equation 10. The implementation of the optimization process remains the same as in Equation 7:

$$L = AEDP^{-1} + \lambda_{MSE} MSE(x, \hat{x}) \quad (10)$$

Table 8 presents the changes in MSE and AEDP for different α values. The first column of Figure 5 illustrates how MSE varies with AEDP, which aligns with the trend observed in the second column of Figure 4 (i.e., Equation 7)—MSE decreases as AEDP increases. Additionally, the second column of Figure 5 shows the contribution of $AEDP^{-1}$ to Equation 10 during the optimization process. Even when magnified 1000 times, its proportion remains negligible. Based on these observations, we conclude that MSE consistently dominates the optimization process, and its reduction is directly caused by the increase in AEDP. Combined with the experimental results of the optimization based on Equation 7, we conclude that the enhanced separability among local representations directly leads to improved reconstruction performance in SAE.

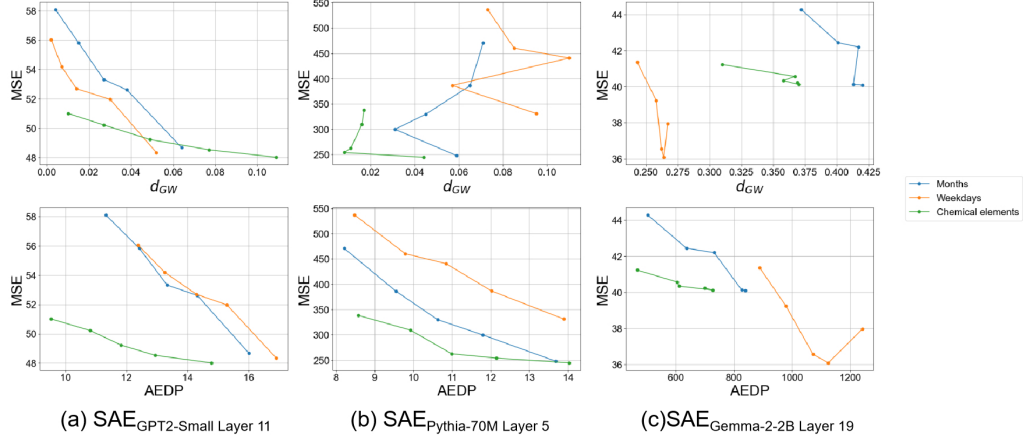


Figure 4: Variability of d_{GW} and AEDP with MSE for different α during the optimization of Equation 7.

Table 8: Variations of MSE and AEDP corresponding to different translation step sizes (α) during optimization based on Equation 10.

Concept	α	SAE _{GPT2-Small Layer 11}				SAE _{Pythia-70M Layer 5}				SAE _{Gemma-2-2B Layer 19}			
		MSE↓	Orig. AEDP	AEDP↑	AEDP ⁻¹ ↓	MSE↓	Orig. AEDP	AEDP↑	AEDP ⁻¹ ↓	MSE↓	Orig. AEDP	AEDP↑	AEDP ⁻¹ ↓
Months	0.5	58.16	10.50	11.32	0.0883	434.09	7.19	8.21	0.1218	44.33	358.97	503.24	0.0020
	0.8	54.90	10.50	12.40	0.0806	383.16	7.19	9.56	0.1046	42.42	358.97	637.58	0.0016
	1.0	54.24	10.50	13.32	0.0751	337.16	7.19	10.63	0.0941	40.91	358.97	730.67	0.0014
	1.2	50.74	10.50	14.31	0.0699	298.28	7.19	11.81	0.0847	40.28	358.97	793.36	0.0013
	1.5	49.72	10.50	16.00	0.0625	231.63	7.19	13.72	0.0729	40.14	358.97	973.32	0.0010
Weekdays	0.5	55.67	11.58	12.21	0.0819	533.29	7.46	8.35	0.1198	40.78	774.53	888.47	0.0011
	0.8	54.48	11.58	13.46	0.0743	496.42	7.46	9.35	0.1070	38.45	774.53	995.49	0.0010
	1.0	52.92	11.58	14.31	0.0699	415.42	7.46	10.86	0.0921	40.36	774.53	1050.32	0.0010
	1.2	51.17	11.58	15.28	0.0654	405.19	7.46	12.01	0.0833	36.41	774.53	1152.77	0.0009
	1.5	48.07	11.58	16.91	0.0591	349.96	7.46	13.91	0.0719	36.45	774.53	1241.62	0.0008
Chemical Elements	0.5	51.27	8.49	9.32	0.1073	343.42	7.53	8.58	0.1166	41.94	318.12	467.35	0.0021
	0.8	49.74	8.49	10.81	0.0925	304.37	7.53	9.92	0.1008	40.63	318.12	604.37	0.0017
	1.0	49.50	8.49	11.82	0.0846	284.00	7.53	10.97	0.0912	40.62	318.12	612.15	0.0016
	1.2	48.29	8.49	12.55	0.0797	252.52	7.53	12.16	0.0822	40.35	318.12	648.64	0.0015
	1.5	47.33	8.49	14.75	0.0678	232.69	7.53	14.01	0.0713	40.87	318.12	945.88	0.0011

B.4.3 Discussion of the results of the experiment in Case 3

The reconstruction error of the three pretrained SAEs exhibits a certain degree of negative correlation with the scale of the corresponding language models. In other word, the larger the language model, the better the reconstruction performance. This stems from the conflict between sparsity and reconstruction performance. The activation frequency of *SAE Pythia 70M Layer 5* is approximately 0.000026%, that of *SAE GPT2 – Small Layer 11* is approximately 0.0039%, and the activation proportion of *SAE Gemma – 2 – 2B Layer 19* is approximately 0.03%, indicating that higher sparsity leads to poorer reconstruction performance. The expansion factor in Table 3 serve as indicators to trade off sparsity and representational performance. Although larger expansion factors may slightly degrade reconstruction performance, our finding regarding the causality between the separability of local representations and reconstruction performance suggests that larger expansion factors also offer greater potential for improving reconstruction performance.

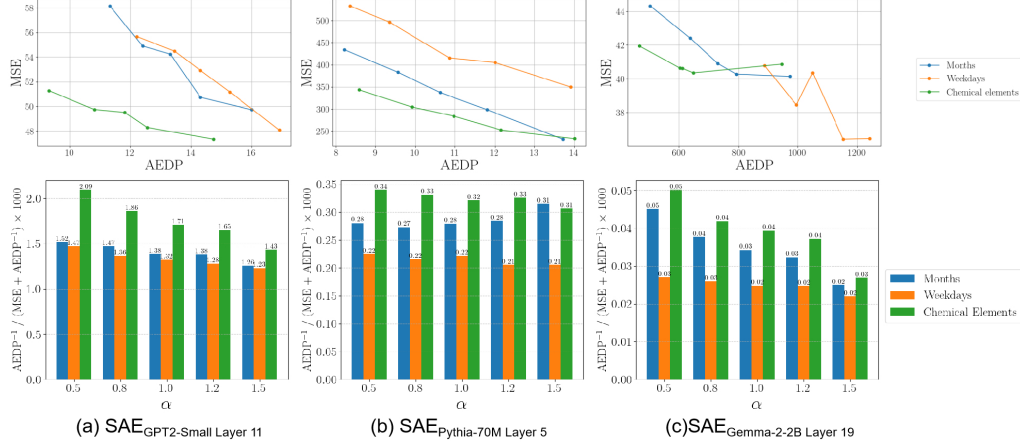


Figure 5: First column: Variability of MSE with AEDP as α increases during the optimization of Equation 10; Second column: Contribution of the $AEDP^{-1}$ term to the Total Loss during the optimization of Equation 10.

C Evaluation Metrics

Average Intrinsic Dimensionality (Avg. ID) [45] Measures the effective dimensionality of local representations, reflecting degrees of freedom introduced by sparse encoding, computed via PCA eigenvalues.

$$ID(\mathcal{M}_c^{(k)}) = \sum_{j=1}^d \mathbb{1}_{\left(\frac{\lambda_j}{\sum_i \lambda_i} > \tau_{\text{dim}}\right)}, \quad \text{Avg. ID} = \frac{1}{K} \sum_{k=1}^K ID(\mathcal{M}_c^{(k)}).$$

where λ_j are eigenvalues of the cluster \mathcal{C}_k covariance matrix, $\tau_{\text{dim}} \approx 0.01$, and K is the number of clusters.

Betti 0 [46] Counts the connected components in a local representation, assessing the topological impact of sparse encoding.

$$\text{Betti}_0(\mathcal{M}_c^{(k)}) = |\{H_0 \text{ bars with length} > \tau_{\text{pers}}\}|, \quad \text{AvgBetti}_0 = \frac{1}{K} \sum_{k=1}^K \text{Betti}_0(\mathcal{M}_c^{(k)}).$$

where H_0 is the 0-dimensional persistence diagram, and $\tau_{\text{pers}} \approx 0.1$.

Minimum Spanning Tree Weight (MSTW) [47] Quantifies the dispersion of cluster centroids in the global representation, computed as the sum of edges in the minimum spanning tree.

$$\text{MSTW}(\mathcal{G}_c) = \sum_{e \in E} \|\mathbf{c}_i - \mathbf{c}_j\|_2.$$

where \mathbf{c}_k is the centroid of cluster \mathcal{C}_k , and E is the edge set of the minimum spanning tree.

Average Geodesic Distance (AGD) [48] Measures geometric differences between SSPD matrices on the manifold, validating representation stability.

$$d_{\text{geo}}(S_m, S_n) = \sqrt{\text{tr}(S_m) + \text{tr}(S_n) - 2\text{tr}\left((S_m^{1/2} S_n S_m^{1/2})^{1/2}\right)}, \quad \text{AGD} = \frac{1}{N(N-1)/2} \sum_{m < n} d_{\text{geo}}(S_m, S_n).$$

where S_m are SSPD matrices, and N is the number of samples.

Procrustes Disparity Compares geometric rearrangement of centroid sets before and after sparse encoding, using Procrustes analysis.

$$\text{Procrustes Disparity} = \min_{R, T} \sum_{k=1}^K \|\mathbf{c}_k^{\text{resid}} - (R\mathbf{c}_k^{\text{latent}} + T)\|_2^2.$$

where $\mathbf{c}_k^{\text{resid}}$ and $\mathbf{c}_k^{\text{latent}}$ are centroids of residual stream and latent tensor, respectively, and R, T are rotation and translation matrices.

The Average Euclidean Distance between Pairs (AEDP) of cluster centers is used to quantify the separability between different local representations.

$$\text{AEDP} = \frac{2}{K(K-1)} \sum_{i < j} \|\mathbf{c}_i - \mathbf{c}_j\|_2$$

where \mathbf{c}_i and \mathbf{c}_j are the centers of clusters i and j , K is the number of clusters, and $\|\cdot\|_2$ denotes the Euclidean norm.

Mean Squared Error (MSE) [49] is introduced to quantify the reconstruction performance of SAEs.

$$\text{MSE} = \frac{1}{N} \sum_{i=1}^N (\hat{x}_{\text{interv}} - x)^2$$

where \hat{x}_{interv} is the reconstructed residual generated by decoding the intervened latent representation through the SAE, and x is the original residual stream.

D Limitations

Although we have confirmed that the representation structure of SAEs pre-trained on the residual stream of language models is stratified, the extraction of activations depends on prompts related to the concept. Despite designing prompts to be as diverse and information-dense as possible, there is still no guarantee that all representations of the concept have been captured (which remains an open problem). Therefore, the rigor of the conclusions needs to be further examined. Additionally, regularization serve as a critical component of SAEs, serve as a role in controlling sparsity. However, in this work, we do not included as a controlled variable. Thus, the differences in representation structure caused by variations in regularization require further exploration.

E Impact Statement

Our paper explains how Sparse Autoencoders (SAEs) organize the representations of activation vectors in language models from the perspective of representation geometry. It reveals the mechanism by which SAEs achieve feature disentanglement from the representation level for the first time. In addition, demonstrates a causal relationship between the separability of local representations and reconstruction performance, advancing research in mechanistic interpretability. As a foundational research, this work provides a reference for developing new neural network decomposition paradigms and optimizing SAEs, without direct societal impact.

F Reproducibility

Algorithm 1 Pseudocode for Case 1

```
1: Input:
2:   Models:  $\mathcal{M} = \{\text{GPT2-Small L11, Pythia-70M L5, Gemma-2-2B L19}\}$ 
3:   Concepts:  $\mathcal{C} = \{\text{Months, Weekdays, Elements, } \dots\}$ 
4:   Noise levels:  $\mathcal{N} = \{0.0, 0.02, 0.05, 0.1, 0.2, 0.5, 1.0, 2.0, 5.0, 10.0\}$ 
5:   Max features:  $d_{\max} = 2048, \epsilon = 10^{-5}, \text{top } k = 100$ 
6: Output: Ranks  $\{r_1, r_2, r_3\}$ , AGD per model, concept, noise level
7: for each  $c \in \mathcal{C}$  do
8:   for each  $m \in \mathcal{M}$  do
9:     Load model  $m$ , SAE, prompts  $P_c$ 
10:    Tokenize:  $\text{tokens} \leftarrow \text{Tokenize}(P_c)$ 
11:    Extract residual:  $\text{resid} \leftarrow \text{SAEMA.extract\_activations}(\text{tokens})$ 
12:    if  $\text{resid} \neq \text{None}$  then
13:      for each  $\sigma \in \mathcal{N}$  do
14:        Add noise:  $\text{noisy\_resid} \leftarrow \text{resid} + \text{Noise}(\sigma, k, 2\sigma, 0.2\sigma)$ 
15:        Encode:  $\mathcal{F} \leftarrow \text{SAE.encode}(\text{noisy\_resid})$ 
16:        Unfold  $\mathcal{F}$ :  $F^{(i)} \leftarrow \text{Unfold}(\mathcal{F}, \text{mode} \in \{\text{batch, seq, feature}\})$ 
17:        Compute SSPD:  $S^{(i)} \leftarrow \frac{F^{(i)} F^{(i)T} + (F^{(i)} F^{(i)T})^T}{2} + \epsilon I$ 
18:        SVD:  $r_i \leftarrow \sum_j \mathbb{1}\left(\frac{\lambda_j}{\lambda_1} > \text{Q1}(\{\lambda_j/\lambda_1 \mid \lambda_j > 10^{-6}\lambda_1\})\right)$ 
19:        AGD:  $\text{AGD} \leftarrow \frac{1}{N(N-1)/2} \sum_{m < n} \|\mathcal{F}_m - \mathcal{F}_n\|_2$ 
20:        Store:  $\text{Results}[c][m][\sigma] \leftarrow \{r_1, r_2, r_3, \text{AGD}\}$ 
21:      end for
22:    end if
23:  end for
24: end for
25: Evaluate: Output  $r_3$  variability, AGD per  $c, m, \sigma$ 
```

Algorithm 2 Pseudocode for Case 2

```
1: Input:  
2:   Models:  $\mathcal{M} = \{\text{GPT2-Small L11, Pythia-70M L5, Gemma-2-2B L19}\}$   
3:   Concepts:  $\mathcal{C} = \{\text{Months, Weekdays, Elements}\}$   
4:   Zero-noise latents  $\mathcal{F}$  and tokens from Case 1 cache  
5:   HDBSCAN min size: 10, UMAP:  $n_{\text{comp}} = 50$   
6: Output: Cluster counts, Avg. ID, Betti 0, MST Weight, Procrustes  
7: Extract residuals:  $\text{resid} \leftarrow \text{SAEMA.extract}(\text{tokens})$  for  $\mathcal{C}, \mathcal{M}$   
8: Initialize Results  $\leftarrow []$   
9: for  $c \in \mathcal{C}$  do  
10:   for  $m \in \mathcal{M}$  do  
11:     if  $\mathcal{F}_{c,m}, \text{resid}_{c,m} \neq \text{None}$  then  
12:       Flatten:  $\text{resid} \leftarrow \text{reshape}(\text{resid}_{c,m}, (-1, d_{\text{model}}))$   
13:       latents  $\leftarrow \text{reshape}(\mathcal{F}_{c,m}, (-1, d_{\text{sae}}))$   
14:       Normalize:  $\text{resid}, \text{latents} \leftarrow \text{Scale}(\cdot) / \|\cdot\|_2$   
15:       Reduce:  $\text{resid}, \text{latents} \leftarrow \text{UMAP}(\cdot)$   
16:       Cluster:  $\text{labels}_{\text{resid}}, n_{\text{resid}} \leftarrow \text{HDBSCAN}(\text{resid})$   
17:        $\text{labels}_{\text{latents}}, n_{\text{latents}} \leftarrow \text{HDBSCAN}(\text{latents})$   
18:       Local:  
19:       for  $l$  in  $\text{labels}_{\text{resid}} \setminus \{-1\}$  do  
20:          $\text{dims}_{\text{resid}}[l] \leftarrow \text{TwoNN}(\text{resid}[l])$   
21:          $\text{beti0}_{\text{resid}}[l] \leftarrow \text{Ripser}(\text{resid}[l], \text{dim} = 0)$   
22:       end for  
23:       for  $l$  in  $\text{labels}_{\text{latents}} \setminus \{-1\}$  do  
24:          $\text{dims}_{\text{latents}}[l] \leftarrow \text{TwoNN}(\text{latents}[l])$   
25:          $\text{beti0}_{\text{latents}}[l] \leftarrow \text{Ripser}(\text{latents}[l], \text{dim} = 0)$   
26:       end for  
27:        $\text{avg\_dim} \leftarrow \text{Mean}(\text{dims}_{\text{resid}}), \text{Mean}(\text{dims}_{\text{latents}})$   
28:        $\text{avg\_beti0} \leftarrow \text{Mean}(\text{beti0}_{\text{resid}}), \text{Mean}(\text{beti0}_{\text{latents}})$   
29:       Global:  
30:        $\text{mst} \leftarrow \text{MST}(\text{labels}_{\text{resid}}, \text{resid}), \text{MST}(\text{labels}_{\text{latents}}, \text{latents})$   
31:        $\text{procrustes} \leftarrow \text{Procrustes}(\text{centers}_{\text{resid}}, \text{centers}_{\text{latents}})$   
32:       Store: Results  $\leftarrow \{c, m, n_{\text{resid}}, n_{\text{latents}}, \text{avg\_dim}, \text{avg\_beti0}, \text{mst}, \text{procrustes}\}$   
33:     end if  
34:   end for  
35: end for
```

Algorithm 3 Pseudocode for Case 3

```
1: Input:
2:   Models:  $\mathcal{M} = \{\text{GPT2-Small, Pythia-70M, Gemma-2-2B}\}$ 
3:   Concepts:  $\mathcal{C} = \{\text{Months, Weekdays, Elements}\}$ 
4:   Case 1 cache: Latents  $\mathcal{F}$ , tokens
5:   Case 2 cache: Residuals, labels
6:   Scales:  $\alpha \in \{0.5, 0.8, 1.0, 1.2, 1.5\}$ 
7: Output: MSE, AEDP per  $c, m, \alpha$ , intervention
8: Load caches: latents, tokens, residuals, labels
9: Results  $\leftarrow \emptyset$ 
10: for  $c \in \mathcal{C}, m \in \mathcal{M}$  do
11:   if data complete then
12:     Load model, SAE, mask  $\leftarrow \text{SAEMA}(\text{tokens})$ 
13:     for intervention  $\in \{\text{GW}, \text{AEDP}^{-1}\}, \alpha \in \{0.5, 0.8, 1.0, 1.2, 1.5\}$  do
14:       centers  $\leftarrow \text{mean}(\text{latents}[\text{labels}])$ 
15:       aedporig  $\leftarrow \text{Mean}(\text{ot.dist}(\text{centers}))$ 
16:       best_latents  $\leftarrow \text{latents}, \text{best\_loss} \leftarrow \infty$ 
17:       for  $i = 1$  to 10 do
18:         new_latents  $\leftarrow \text{latents} + (\text{centers} - \text{mean})$ 
19:         aedp  $\leftarrow \text{Mean}(\text{ot.dist}(\text{centers}))$ 
20:         mse  $\leftarrow \text{Mean}((\text{SAE}(\text{new\_latents}) - \text{resid}_{\text{masked}})^2)$ 
21:         loss  $\leftarrow \begin{cases} \text{ot.gromov\_wasserstein2}(\text{dist}_{\text{orig}}, \text{dist}_{\text{new}}) + \text{mse}, & \text{if GW} \\ \frac{1}{\text{aedp}} + \text{mse}, & \text{if AEDP}^{-1} \end{cases}$ 
22:         if loss < best_loss then
23:           best_latents  $\leftarrow \text{new\_latents}, \text{best\_aedp} \leftarrow \text{aedp}$ 
24:         end if
25:         centers  $\leftarrow \text{centers} + \alpha \cdot \text{random\_grad}$ 
26:       end for
27:       mse  $\leftarrow \text{Mean}((\text{SAE}(\text{best\_latents}) - \text{resid}_{\text{masked}})^2)$ 
28:       Results  $\leftarrow \{c, m, \text{intervention}, \alpha, \text{mse}, \text{aedp}_{\text{orig}}, \text{best\_aedp}\}$ 
29:     end for
30:   end if
31: end for
```
